



Activated carbon-supported NiS/CoS photocatalyst for degradation of methyl violet (MV) and selective disinfection process for different bacteria under visible light irradiation

Öge Artagan, Ali İmran Vaizoğullar & Mehmet Uğurlu

To cite this article: Öge Artagan, Ali İmran Vaizoğullar & Mehmet Uğurlu (2021) Activated carbon-supported NiS/CoS photocatalyst for degradation of methyl violet (MV) and selective disinfection process for different bacteria under visible light irradiation, Journal of Taibah University for Science, 15:1, 154-169, DOI: [10.1080/16583655.2021.1930718](https://doi.org/10.1080/16583655.2021.1930718)

To link to this article: <https://doi.org/10.1080/16583655.2021.1930718>



© 2021 The Author(s). Published by Informa UK Limited, trading as Taylor & Francis Group.



Published online: 28 May 2021.



Submit your article to this journal [↗](#)



Article views: 59



View related articles [↗](#)



View Crossmark data [↗](#)

Activated carbon-supported NiS/CoS photocatalyst for degradation of methyl violet (MV) and selective disinfection process for different bacteria under visible light irradiation

Öge Artagan^a, Ali İmran Vaizoğullar^a and Mehmet Uğurlu^b

^aVocational School of Health Care, Medical Laboratory Program, Muğla Sıtkı Koçman University, Muğla, Turkey; ^bFaculty of Science, Department of Chemistry, Ağrı İbrahim Çeçen University, Ağrı, Turkey

ABSTRACT

The activated carbon (AC) supported sulphur-based Ni/Co photocatalysts were prepared using the simple chemical precipitation method. The prepared samples were characterized with advanced scanning electron microscope, x-ray diffraction, Raman, UV-DRS, PL analyses. SEM images presented that AC-supported NiS and CoS nanocomposites were spherical and had rod-like morphologies. To determine photocatalytic performance and the kinetic model, the decomposition of Methyl Violet (MV) was carried out on all the photocatalyst samples. The synergetic effect was performed by comparing NiS/AC, CoS/AC and Ni/CoS/AC composites. The photocatalytic yield of the Ni₇Co₃/AC nanocomposite sample towards (MV) was found to be 98% in 90 min also under the same experimental conditions other AC-supported samples which CoS/AC, NiS/AC, and Ni₃Co₇/AC showed 56%, 74% and 78% photodegradation efficiency, respectively. The obtained results showed that the optimal content of component affects the degradation ability and also composites with increased NiS content displaying better photocatalytic performance. Ni₇Co₃/AC inactivation performance against *S. aureus* and *E. faecalis* was outstanding; nearly 100% inactivation was attained in less than 2 h. *S. aureus* and *E. faecalis* are both Gram positive (Gr+) bacteria. The Ni₇Co₃/AC composite deactivated Gr+ bacteria but had no effect against Gr- bacteria during the incubation period.

ARTICLE HISTORY

Received 14 February 2021
Revised 24 March 2021
Accepted 29 March 2021


KEYWORDS

NiS/CoS; Gr+ bacteria;
organic pollutant; activated
carbon

1. Introduction

Disinfection is recognized as an effective technique for reducing pathogens and protecting people against waterborne infectious diseases. Chemical disinfection, especially chlorination is the most popular sterilization technique used for water purification [1–3]. However, evidences show that the chlorine residue poses a serious public health risk [4]. Traditional disinfection methods such as chlorination, UV irradiation and ozonation can produce serious problems such as insufficient wastewater treatment, incomplete removal of colours, high energy requirement, phase production containing secondary pollutants and fluctuations [5–7]. Recently, industrial waste waters or other samples/contaminants such as toxic heavy metals which are mutagenic, carcinogenic and toxicity depend strongly on their oxidation state and colour [8]. This contamination will become a major problem for human health [9]. Many industrial wastes originating from the textile, food, leather industry, etc. contain azo dyes or toxic organic compounds. These compounds also show durability in degradation processes due to their chemical structure [10]. The colour removal from waste water has attracted more attention than other colourless wastes since it is toxic and an indicator of polluted water [11]. There

are many different azo dyes. However, some dyes are extremely toxic, stable and too difficult to degradation such as Methyl Violet (MV) which contains some mixtures of tetramethyl, pentamethyl and hexamethyl pararosanilins. This substance is found in wastewater of textile or other industrial sectors. MV requires high chemical oxygen demand (COD) in aqueous environment. Furthermore, chemicals such as benzamine that result from chemical reactions can cause cancer in humans [12]. Physical, chemical or biological methods are used in the treatment of wastewater. However, these methods either create secondary pollution or cannot provide adequate removal. In this respect, it becomes necessary to implement an advanced treatment process of MV. The advanced oxidation process (AOP) can be thought in two subgroups as homogeneous and heterogeneous. Based on hydroxyl radicals, it provides the complete mineralization of organic compounds. The radicals formed on semiconductors by the effect of light attack organic compounds and oxidize them to CO₂ and H₂O [13]. The degradation of organic toxic dyes with an advanced oxidation technique has recently attracted the attention of researchers due to its low cost, continuity and ease of application. This advanced oxidation technique is a chemical method

CONTACT Ali İmran Vaizoğullar  aliimran@mu.edu.tr

© 2021 The Author(s). Published by Informa UK Limited, trading as Taylor & Francis Group.

This is an Open Access article distributed under the terms of the Creative Commons Attribution License (<http://creativecommons.org/licenses/by/4.0/>), which permits unrestricted use, distribution, and reproduction in any medium, provided the original work is properly cited.

that provides the oxidation of toxic components to non-toxic carbon dioxide or other inorganic molecules with the help of a semiconductor photocatalyst. Recently some materials have been synthesized for the degradation of MV. These materials showed degradation efficiency up to 95% [14,15]. However, sulphur-based materials have also been used very frequently due to their unique properties such as solar energy storage cell, high electrical conductivity, sensors, photocatalysis and chemical sensing ability [16]. For example, NiS can be used in a wide variety of fields such as optical and magnetic properties energy storage and sensors since it has a wide absorption feature in the solar spectrum. Due to the low band gap energy, which is an important criterion especially in photocatalytic reactions, it can also be applied under visible light. However, low band gap energy cannot be a positive effect immediately. Because the rapid recombination of excited electrons and holes shows an inefficient photocatalytic performance. Materials must be subjected to some modifications to overcome such difficulties. Similarly, CoS, which has different chemical formulas such as CoS or Co₃S₄, is used in various fields due to its optical and electronic properties. As known, in a semiconductor material, an important drawback is the electron/hole recombination causing to consume the energy as heat and a major decrease in the photocatalytic degradation [17]. Supporting or coupling of p-n, p-p and n-n composite photocatalysts are an effective process to destroy toxic compounds. Where the excited electrons can migrate to the CB level of other semiconductor to decrease recombination rate of electron/hole pairs. Also, the holes are moved in the opposite direction between VB levels. This charge transferring strongly inhibits the electron/hole pairs resulting in a major increase in the photocatalytic degradation activity [18–20]. Also, supporting of a semiconductor material onto a clay mineral fine disperses them and inhibits their aggregation. The obtained high surface area provides more quantitative photons resulting in higher charge carriers. This also prevent the collisions of semiconductors with ground state to enhanced recombination of electron/hole blocking [21,22]. Considering some working examples of sulphur-based nickel and cobalt composites Borthakur and Das [23] synthesized the NiS₂/CoS/AC material by the hydrothermal method and used it in the degradation of MV. They reported the use of graphite oxide to prevent aggregation of the material. In addition, they investigated the effects of the surface load of the material on the catalytic activity. Yang and co-workers [24] synthesized NiS/CoS/AC composites and used it in hydrogen evaluation reactions. From the findings/according to results, they stated that three-dimensional composites have longer diffusion efficiency and electronic conductivity. In addition, pathogenic species such as bacteria, viruses and protozoa have been a major environmental and human health risk [25]. Therefore, an effective method

with high performance, low energy has become mandatory for disinfection of bacteria.

Until now, there is no report of sulphide-based NiS/CoS/AC composites for the decomposition of organic pollutants and disinfection studies. Also, in photocatalytic studies of sulphur-based nickel and cobalt, activated carbon (AC) was presented for the first time in this study. In the present study, the degradation performance of NiS/CoS/AC composites for MV dye was studied. The photocatalytic degradation performance of composites (NiS/AC, CoS/AC and composites which contain different amounts of NiS and CoS) was compared between NiS/AC, CoS/AC and composites. The composites are defined as Ni₃Co₇/AC and Ni₇Co₃/AC. Also the most photocatalytic active composite sample Ni₇Co₃/AC was chosen for the disinfection process against four different microorganisms (*Staphylococcus aureus* ATCC 25923, *Escherichia coli* ATCC 25922, *Pseudomonas aeruginosa* ATCC 27853, and *Enterococcus faecalis* ATCC 29210). This study also aims to develop a selectively sensitive composite material for photocatalytic applications. With this effect, a controllable chemical reaction will play a major role in the synthesis and application of materials with the desired physicochemical properties with a simple method.

2. Materials and methods

2.1. Preparation of photocatalysts

All materials were synthesized using chemical precipitation and a co-precipitation method. Simply, 5.6 g of Ni(Cl)₂·6H₂O was dissolved in 50 ml of water and then 1.12 g of Na₂S was added to this solution slowly and stirred for 1 h. The obtained black powder was filtered and dried at 80°C for 2 h. Similarly, 5.1 g of Co(NO₃)₂·2H₂O was dissolved in 50 ml of water. Then 1.16 g of Na₂S was added to this solution slowly to obtain black CoS powders for 1 h. The powders were then dried at 80°C for 2 h. To prepare the NiS/CoS/AC composite samples 2 g of AC and 2.4 g of NiS (aqueous suspension, where the concentration was estimated on the basis of dry powders) and a desired amount of Co(NO₃)₂·2H₂O was dissolved in 50 ml of distilled water and then stirred for 2 h. After that a stoichiometric calculated amount of Na₂S was added into the solution with vigorous stirring. Finally, the obtained black powders were collected and washed with distilled water five times. The obtained composites were filtered and then dried at 80°C for 2 h. In the synthesis of all photocatalysts, the amount of activated carbon (AC) used was 2 g.

2.2. Characterization

The morphological structures of the particles were investigated using scanning electron microscope (SEM)

(JEOL JSM-7600F). The crystalline structures were investigated by x-ray diffraction (XRD: Rigaku D/MAX 350) using copper K radiation ($k = 0.15401$ nm). X-ray photoelectron spectroscopic (XPS) measurement was performed using a PHI 5000 Versa Probe. The optical properties of the samples (UV-vis DRS) were performed using a Lambda 35 UV-vis spectrophotometer in the solid state. The photoluminescence spectra of photocatalyst samples were observed using spectrofluorometric (Spex 500 M, USA) photoluminescence (PL) emission spectra. The recorded spectra were obtained using 532 nm lasers. The electrochemical impedance spectra (EIS) were analysed on an impedance analyzer (Gamry Potansiyostat/Galvanostat/ZRA Reference 3000) using a standard three-electrode system with the samples as the working electrodes, a saturated calomel electrode as the reference electrode and a Pt wire as the counter electrode, respectively. The frequency operating range was specified as 1 kHz–107 Hz. Raman analyses were studied at room temperature using a Raman spectrophotometer (Bruker IFS 66/S, Fra 106/S, Hyperion 1000, Raman scope II).

2.3. Photocatalytic performance studies

All photocatalytic degradation studies were performed in a beaker (100 ml) at ambient temperature. For irradiation sources, 400 nm of LED lamps (9 W and 3 number) were used. Three different lights were positioned on the beaker at an angle of 120° at a distance of 3 cm from the beaker. To decompose of MV dye under visible light irradiation, 0.5 g of the photocatalyst was added to 100 ml of the MV dye solution (10 ppm). The solution was stirred for 30 min to achieve adsorption/desorption equilibrium. After irradiation, 3 ml of the aliquot was taken to observe the absorption value in a UV-Vis spectrophotometer. MV shows a maximum peak at 528 nm wavelength. Each measurement for residual MV dye and absorbance was carried out once in 30 min. Degradation efficiency was calculated using the below formula;

$$\% \text{Degradation} = \frac{C_0 - C}{C_0} \times 100 = \frac{A_0 - A_t}{A_t} \times 100 \quad (1)$$

where A_0 and A_t are the initial and final absorbencies of MV at 528 nm. According to the Lambert Beer law, the initial and final absorbance values are directly proportional to the initial and final concentrations, respectively.

2.4. Determination of minimum inhibitory concentrations (MIC)

Antibacterial activities against the four bacteria (*S. aureus* ATCC 25923, *E. coli* ATCC 25922, *P. aeruginosa* ATCC 27853 and *E. faecalis* ATCC 29210) were determined by the micro broth dilutions technique using

the Clinical Laboratory Standards Institute (CLSI) recommendations. Mueller–Hinton broth for bacteria were used as the test media. Serial two-fold dilutions of different concentrations were prepared in the medium. Bacteria were adjusted to a turbidity equivalent to the 0.5 McFarland standard, diluted in broth media to give a final concentration of 5×10^5 cfu/ml for the bacteria in the 96-well plates. The plates were incubated at 37°C for 24 h. The MIC was defined as the lowest concentration of the test that produced the complete inhibition of visible growth (CLSI M7-A7, 2006) [26].

2.5. Bacterial strains and growth conditions

Nutrient agar for bacteria (*S. aureus* ATCC 25923, *E. coli* ATCC 25922, *P. aeruginosa* ATCC 27853, and *E. faecalis* ATCC 29210) was prepared and diluted to 25 ml in petri dishes for the purpose of studying the surviving microorganisms. The material was weighed at $4000 \mu\text{g/ml}$ and incubated with microorganisms. At the 2nd and 4th hours samples were taken, incubated in daylight, specimens taken, transferred to new petri dishes and incubated for 24 h at 37°C , then the colony was counted [27].

3. Results and discussion

3.1. SEM analysis

Figure 1 shows typical SEM images of NiS/AC, CoS/AC and Ni7Co3/AC. As seen from Figure 1, NiS/AC and CoS/AC display uniform spherical and very thin morphology with diameters of 30–50 and 50–10 nm, respectively. The nanostructure of the NiS/AC sample takes shape by the assembly of spherical NiS and AC (Figure 1(a)). For the CoS/AC sample, CoS has a nanostructure of nanosheets onto AC (Figure 1(b)). As a result of supporting NiS and CoS on activated carbon (AC), the morphological structure of the materials did not change significantly (Figure 1(c)). Furthermore, the composite Ni7Co3/AC sample is composed of a large amount of bush-like sub units confirming a hierarchical structure. This property is useful for the intimate contact of active sites with the electronic structure to enhance the effective photo electrochemical activity of Ni7Co3/AC [1]. In addition, the use of activated carbon enables the materials to have a larger surface area. Compared to materials with low surface area, it will allow a more efficient photocatalytic reaction by preventing the absence of inter-pore connections that allow percolation to occur [28].

3.2. XRD analysis

To determine phase purity of the composite materials XRD analysis which gives effective information for the crystallite defects, strain and size distribution was

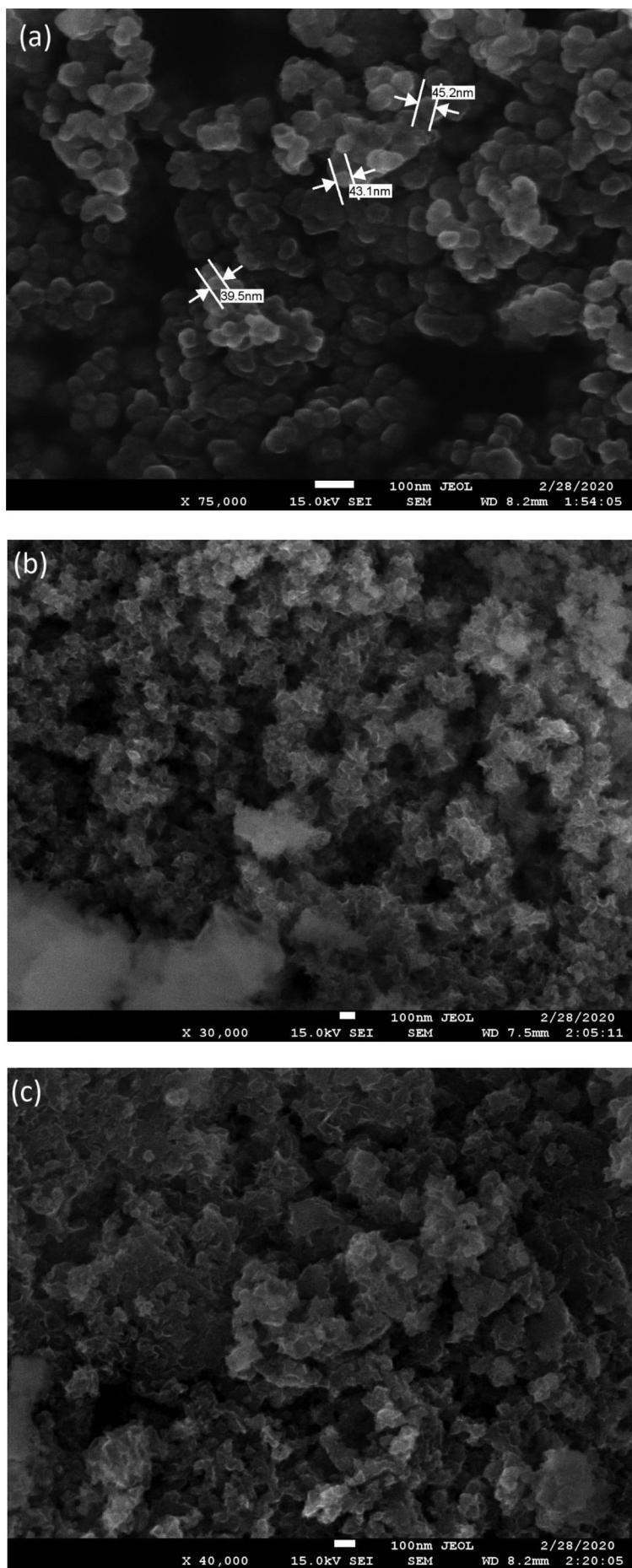


Figure 1. SEM images of all NiS/AC (a) CoS/AC, (b) and Ni₇Co₃/AC (c) photocatalyst sample.

performed. Figure 2 exhibits XRD pattern of all photocatalysis samples. As seen, the diffraction peaks at approximately $2\theta = 23.4^\circ$ can be assigned to the turbostratic graphite structure [29]. Also, five diffraction peaks at $2\theta = 32.20^\circ, 36.44^\circ, 40.45^\circ, 48.52^\circ$ and 60.42° are attributed to (300), (021), (221), (131) and (330) plane of the hexagonal phase of NiS, respectively (JCPDS 75-0613) [30]. In addition, the XRD diffraction peaks of CoS were seen at $2\theta = 30.7^\circ, 34.6^\circ, 53.42^\circ$ which matched with (1 0 0), (1 0 1), and (1 1 0) planes for the hexagonal CoS structure ((JCPDS 65-3418) [31]). These results present an effective AC-supported NiS/CoS composite for MV degradation.

The Williamson-Hall (W-H) method was used to calculate the crystallite size of the NiS and CoS nanoparticles. According to the below formula, β is the full width at half maximum, λ is the Cu- $k\alpha$ radiation wavelength (1.5406 Å), θ the angle, d the crystallite size and μ represents the strain in the crystallite structure. The k value is generally 1 but it can be vary between 0.8 and 1.4. When the strain value is zero, the W-H method converts to the Scherrer equation (Equation (2))

$$\beta \cdot \cos\theta = \left(\frac{k\lambda}{d} \right) + (\mu \cdot \sin\theta) \quad (2)$$

According to the W-H method, the slope of the obtained linear line can be positive or negative. When it is positive, the tensile strain, which can be caused by the relative shift in the peak position by the contact and coherency stresses, grain boundary, triple junction and tacking faults are revealed [32,33]. In the absence of those described above, a negative slope with the present pressure strain is obtained.

If the plot of $\beta \cdot \cos\theta$ versus $\mu \cdot \sin\theta$ is plotted, a straight line must be obtained and the strain from the slope and the crystal size at the intercept are calculated. The obtained W-H plot and intercept in Figure 2(b) shows that the grain size was 21.9 nm.

$$d = \frac{k\lambda}{\beta \cos\theta} \quad (3)$$

The Scherrer equation is presented in Equation (2). Where the grain sizes of nanocomposites are d , k is about 0.9, λ is the Cu- $k\alpha$ radiation wavelength (1.5406 Å) and θ the angle. Based on the information and calculated data, the grain size of Ni7Co3/AC sample is 28.9 nm.

3.3. XPS analysis

The chemical states and surface composition of the Ni7Co3/AC sample was evaluated by XPS. The survey spectra of the composite showed the presence of Ni, Co, S, O and C (Figure 3(a)). Spectral areas of the Ni7Co3/AC sample were fitted by the Gaussian method, and are presented in Figure 3. The peaks located at 860.58 and

878.68 eV correspond to the Ni2p_{3/2} and Ni2p_{1/2} states of Ni²⁺ respectively (Figure 3(a)) [34].

For S2p spectra, as seen, the S2p spectra display three signals. The peak at 161.25 eV assigned to S²⁻ in NiS. The S 2p core level shows large chemical shifts; the peaks at 167.14 and 172.57 eV possibly show other oxidized species such as sulphate or sulphide which are S⁶⁺ and S⁴⁺ respectively [35].

For Co2p XPS spectra, there are two main peaks at 785.24 and 801.25 eV indicating the 2p_{3/2} and 2p_{1/2} Co²⁺ state in the Ni7Co3/AC sample [36]. Figure 3(d) displays the C1s spectra for AC. It is clearly seen that the C1s spectra for AC present two strong peaks at 284.45 and 288.59 ascribed to the sp² carbon and epoxide groups, respectively [37]. All XPS spectra strongly indicate that the high-purity NiS/CoS/AC heterojunction composite was successfully prepared.

3.4. Electrochemical impedance studies

Typical electrochemical impedance results of NiS/AC, CoS/AC and Ni7Co3/AC samples are presented in Figure 4. As known, the arc radius of on the EIS spectra displays resistance of the interface layer at the catalysts' surface resulting in a smaller arc radius confirming the higher charge transfer [38]. It is possible to interpret the data of an electrochemical system (R_s , R_p and C_d) in a certain frequency range. The equation for a simple impedance expression can be written as follows:

$$Z_w = R_s + \left(\frac{R_p}{1 + j\omega R_p C_d} \right) \quad (4)$$

Nyquist and the Bode plots can be significantly used for the impedance data. In the Nyquist plot imaginary numbers $Z(\omega)$ are plotted versus real numbers $Z^l(\omega)$. In the Bode plot, the absolute values of impedance or phase angle are plotted versus the frequency. The frequency-dependent term of the above equation is neglected at very high frequencies. In this case, $Z(\omega) = Z^l(\omega) = R_s$ occurs. When $\omega \rightarrow 0$, in this case, $Z(\omega) = R_s + R_p$ equality occurs. If the following equation is taken into account at the maximum $Z(\omega)$ frequency, a parameter related to the time constant of the electrochemical reaction emerges. This parameter shows the rate of the reaction. Hence, the R_s , R_p and C_d values can be obtained from the Nyquist plot. On the Nyquist plot, the frequency decreases to the left of the x-axis (Equation (5))

$$R_p \cdot C_d = \frac{1}{\omega_{\max}} = \frac{1}{2\pi f_{\max}} = k_{\text{reaction}} \quad (5)$$

At high and low frequencies, the R_s and R_p values estimated from the Nyquist plot can be found from the $Z(\omega)$ versus $\log(\omega)$. When Equation (4) is taken into account, it is verified that the slope is -1 by taking the logarithm of the absolute $Z(\omega)$ versus $\log(\omega)$. Usually a straight line with a slope of -1 in the mid-frequency region can be observed. The intercept point of the line gives the value

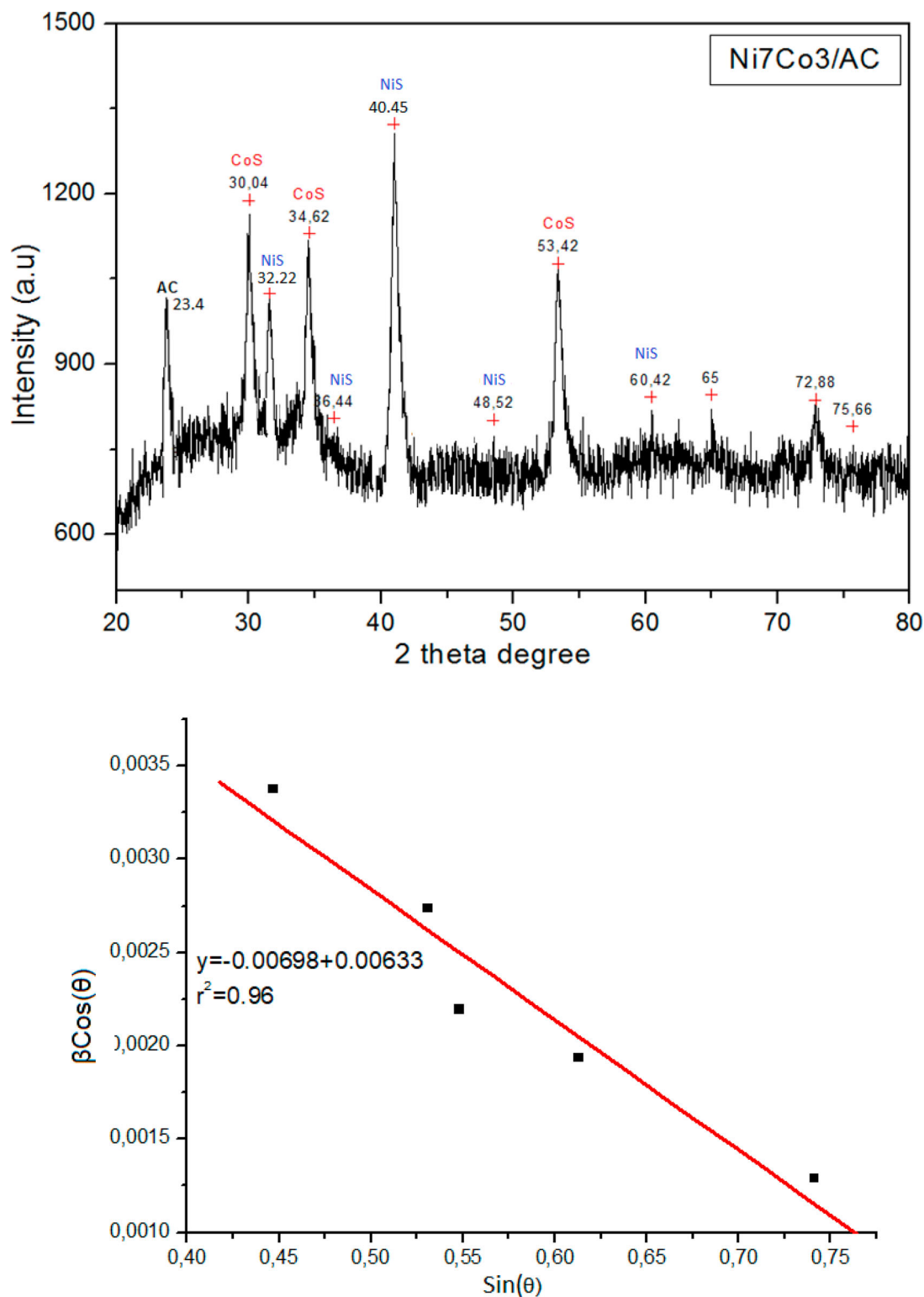


Figure 2. XRD pattern of the Ni7Co3/AC photocatalyst sample. (a) Based on the XRD data of the composite W-H (Williamson–Hall) curve plotted.

of C_d . So the Nyquist and the Bode plots produce similar results [39].

EIS with the Nyquist plot is displayed in Figure 4. As seen, the semicircle radius of the Ni7Co3/AC photocatalyst sample is smaller than that of other photocatalyst samples in the middle-frequency region. It indicates the more efficient inhibition of electron/hole pairs and

faster transportation of photogenerated charge carriers in the Ni7Co3/AC composite [40].

3.5. Raman analysis

Raman studies were evaluated to further reveal the structure characteristics of NiS/AC, CoS/AC and Ni3Co7/AC

photocatalyst samples. As seen from Figure 5 two strong peaks at 1357 and 1576 cm^{-1} are observed indicating well D and G bands, respectively. The D band is attributed to the aromatic structure of sp^3 bonded carbons. Also the G band is attributed to the first-order scattering of the stretching vibration mode of E_{2g} for sp^2 carbon atoms. The peak at 286 cm^{-1} is ascribed to the A vibration mode of $\beta\text{-NiS}$. Also the vibration peak at 495 cm^{-1} defines the Ni(OH)_2 mode [41].

Furthermore, some vibrational modes cannot be observed. We can infer that the small size of materials caused this result since Raman vibrational modes strongly depend on the vibration of the lattice structure. In Raman spectra of the CoS/AC sample the characteristic peaks at 455 , 508 and 652 cm^{-1} show the E_g , F_{2g} and

A_{1g} modes of CoS, respectively [42]. Also, as seen in the NiS/AC sample, the characteristic Raman spectrum of AC is observed in the CoS/AC sample. When considering the Raman spectra of the Ni₇Co₃/AC sample, both characteristic peaks of CoS and NiS were found. It is pointed out that the peaks attributing of NiS at 286 cm^{-1} and of CoS at 652 cm^{-1} are slightly shifts to 288 and 653 cm^{-1} respectively. It can thus be suggested that these opposite shifts definitely show opposite charge transfer due to the formation of heterojunction [43].

3.6. UV-DRS evaluation

The band gap potentials of the samples were estimated by the Kubelka–Munk (Equation (7)). It is shown in

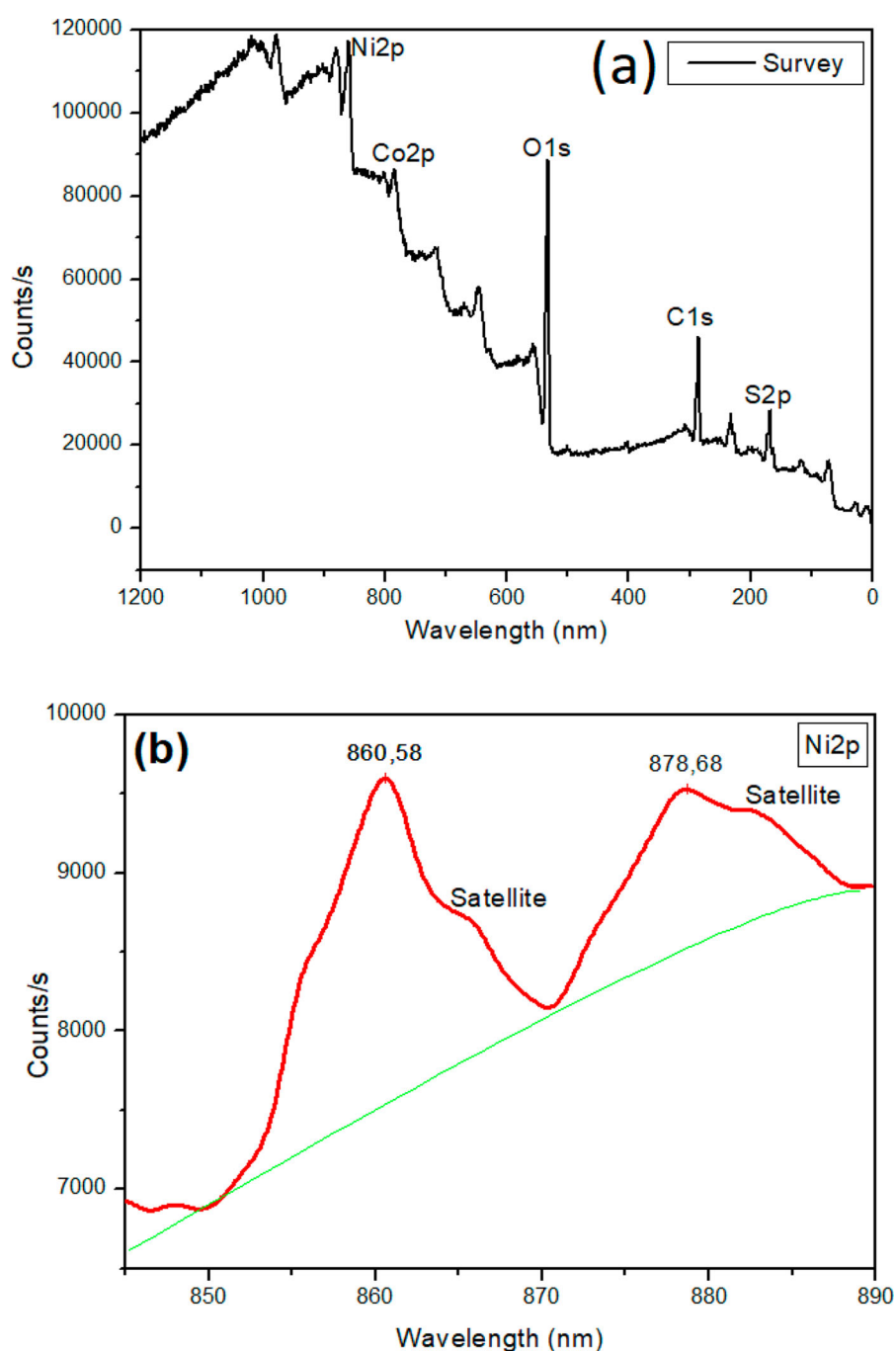


Figure 3. XPS results of Ni₇Co₃/AC sample.

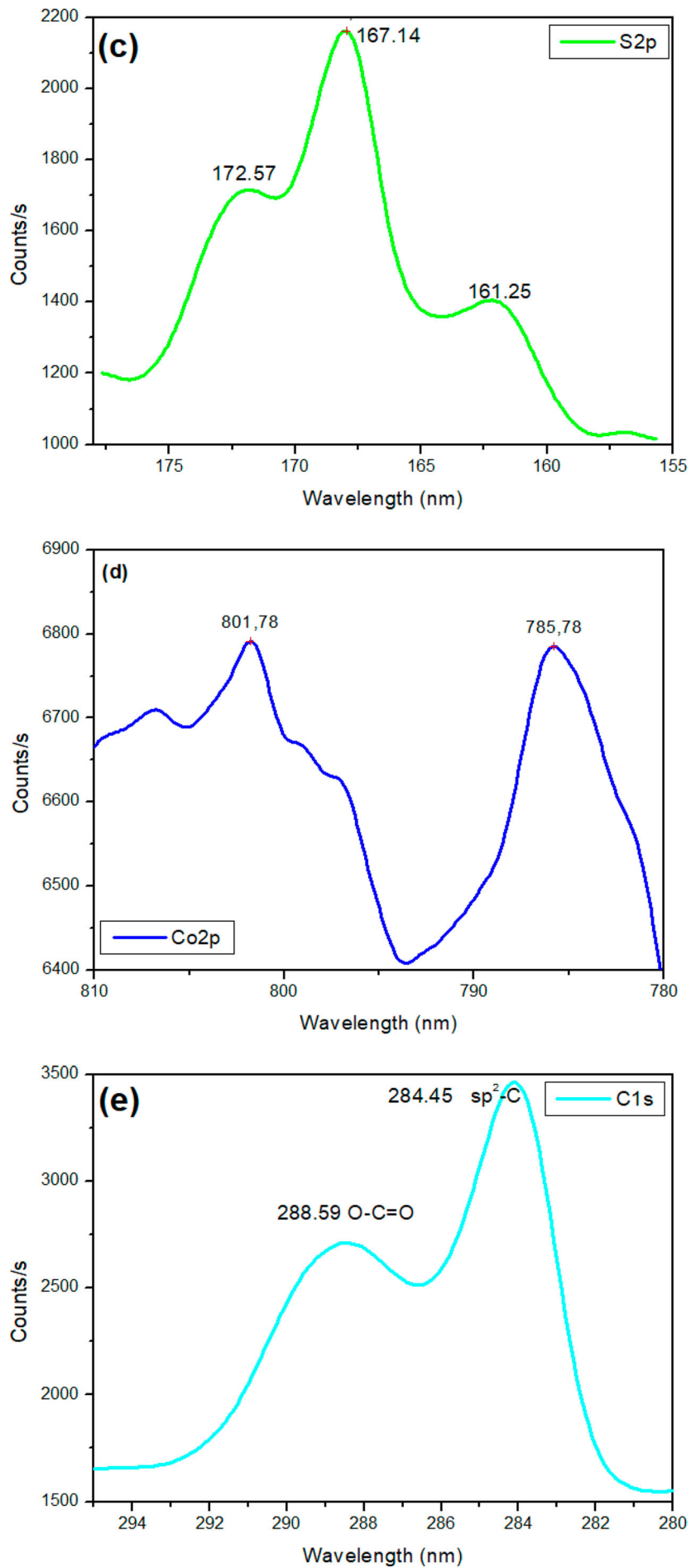


Figure 3. Continued.

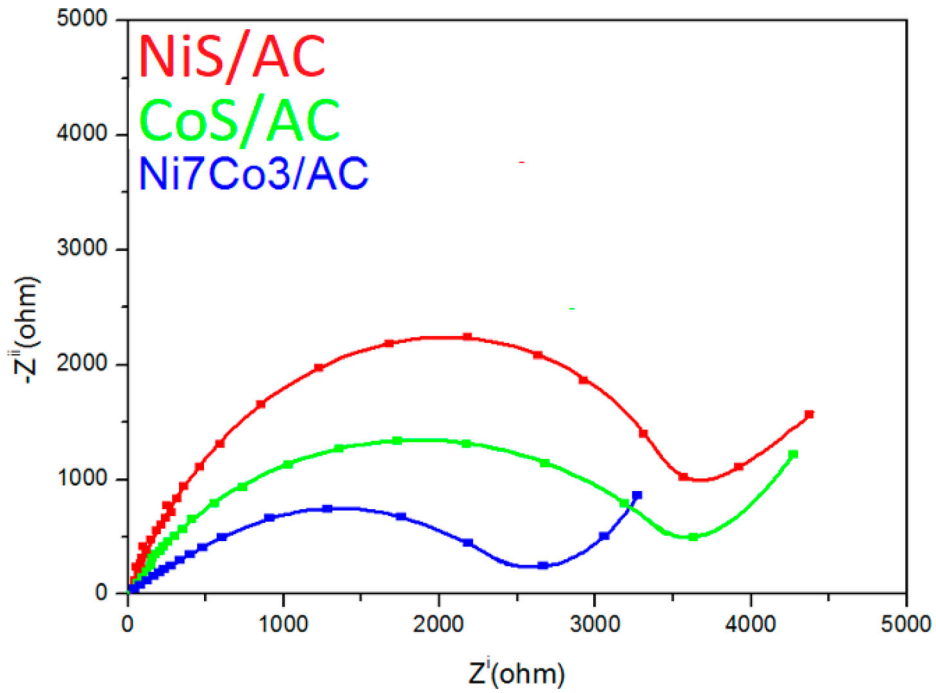


Figure 4. Electrochemical impedance of bare NiS/AC, CoS/AC and Ni7Co3/AC samples.

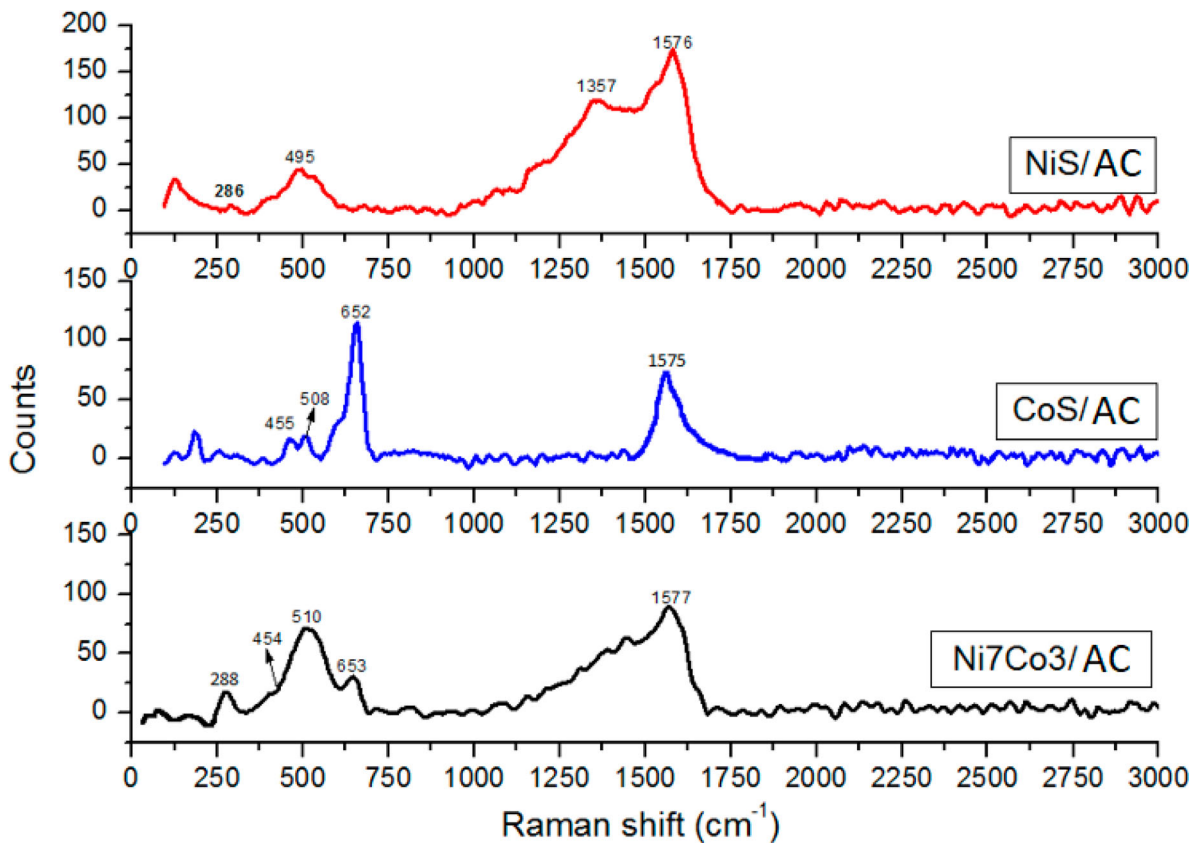


Figure 5. Raman spectra of NiS/AC, CoS/AC and Ni7Co3/AC photocatalyst samples.

Figure 6

$$K = \frac{(1 - R)^2}{2R} \quad (6)$$

K is the reflectance transformed and R is the reflectance (%). In addition, the Tauc plots of direct and indirect band gap values are plotted with $(\alpha h\nu)^2$ and $(\alpha h\nu)^{1/2}$ respectively [44]. The obtained band gaps for the direct

transition was used to find the band edge potentials of the photocatalysts samples using the below equation [45].

$$E_{CB} = \delta - E_E - 0.5 \times E_g \text{ and } E_{VB} = E_{CB} + E_g \quad (7)$$

On the basis of the Pearson Absolute Electronegativity, (δ) is the electronegativity of CoS (5.76 eV) and

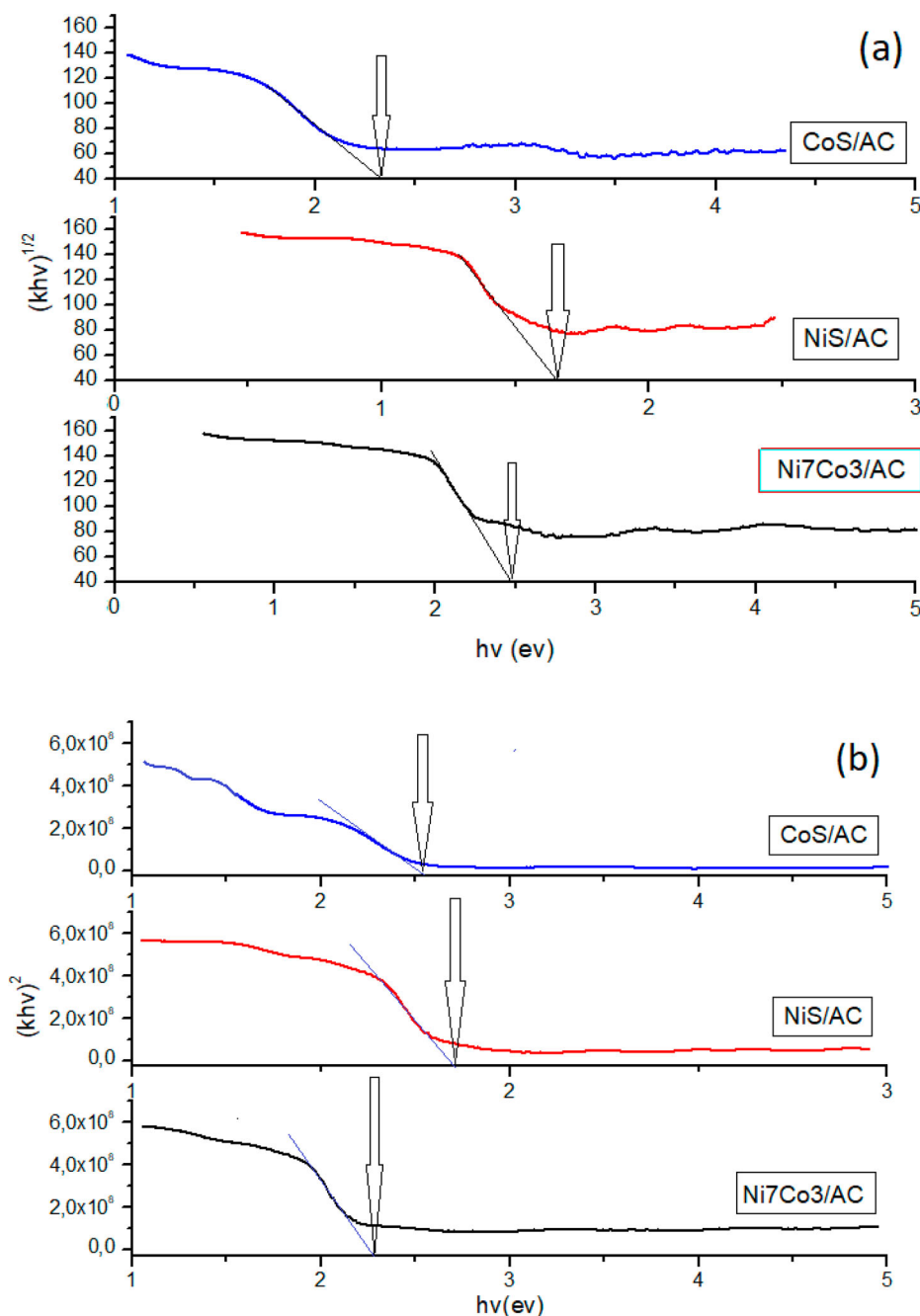


Figure 6. (a and b) Typical Tauc plots for indirect and direct transitions of CoS/AC, NiS/AC and Ni7Co3/AC samples.

NiS (5.71 eV) and E_E is the energy of free electron on the hydrogen scale (NHE, 4.5 eV). E_{CB} , E_{VB} and E_g are conduction band, valence band and band gap values, respectively. The calculated band gap values of E_{CB} , E_{VB} and E_g for CoS and NiS are 0.045, 2.475, 2.42 and 0.32, 2.1, 1.78 eV, respectively. According to these band gap values, the band edge potential scheme is Type 1. For Type 1 heterojunction photocatalysts, the CB and VB levels of CoS are higher than the NiS. Under light irradiation, both electrons and holes will transfer from CoS to NiS.

Figure 7 presents the possible degradation mechanism of the Ni7Co3/AC sample. Firstly, CoS and NiS in the composite structure can be excited by visible light due to its lower band gap energy (2.43 and 1.78 eV

respectively). When the visible light is irradiated onto the composite, both CoS and NiS were excited. The CB band potential of CoS is more electronegative than NiS. Therefore, the excited electrons of CoS could easily transfer to NiS due to intimate contact. Similarly, the holes from CoS can transfer to the VB of NiS band potential level. Where Type I heterojunction had occurred, the redox potential of superoxide radical is -0.33 eV. The CB band potential of the composite is suitable to form superoxide radicals ($O_2^{\bullet-}$) by reacting with (O_2). However, the transferred holes from CoS to NiS could not reveal hydroxide radicals due to less electropositive nature ($OH^-/\cdot OH = 2.40$ eV). This finding is unexpected but suggested that hydroxyl radicals (OH^{\bullet}) may form from superoxide radicals, which are found in the reaction

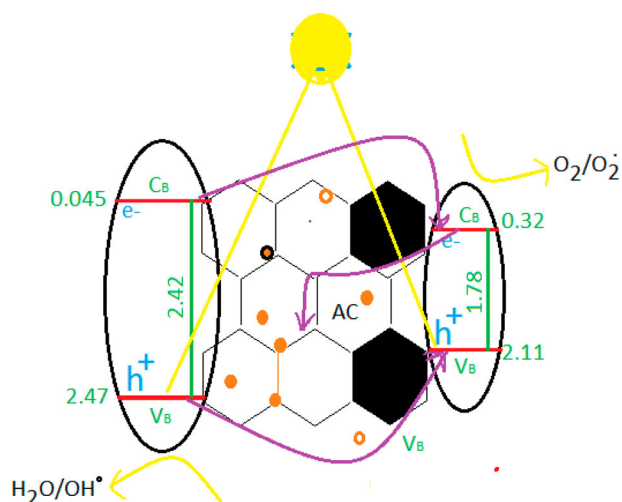


Figure 7. The possible charge transfer pathway in the degradation/disinfection reaction for Ni7Co3/AC.

medium due to both NiS and the transferred electrons of CoS [46]. However, even in small amounts, holes in the VB level of CoS have the potential to generate some hydroxyl radicals. Also, the photon generated electrons in the reaction medium can transfer to the AC surface. Two different electron transfers on this ternary material make a great contribution in blocking recombination of electron/hole pairs, which plays a major role in the photocatalytic degradation. Here, the importance of AC for CoS/NiS, which are a Type I heterojunction composite, emerges. The type 1 heterojunction structure has more recombination rate than the other structures (Type II or Z-Scheme) [47]. In order to make this effective distinction, AC has been considered as the composite within the CoS/NiS structure.

3.7. Photocatalytic degradation of MV

The change in the MV absorbance during irradiation time is presented in Figure 8(a,b). The absorbance of MV under dark conditions increased after remaining constant. After that MV concentration decreased within 90 min, implying the effective degradation for MV. The photocatalytic performance of MV degradation was as follows CoS/AC < NiS/AC < Ni3Co7/AC < Ni7Co3/AC, respectively. As the surface area of AC is high, it is expected that a high absorbance value will be formed in the dark. Under light conditions all photocatalysts samples can absorb photons in the visible light area and also since the band gap energies of the catalyst components are low, very high efficiency degradation has been achieved in the visible region. As seen from Figure 8(a), almost 40–50% of MV is adsorbed on the photocatalyst sample. Some researchers have expressed that the dark adsorption of a dye is attributed to homogeneous monolayer adsorption. However, adsorption in dark environment can not attributed the real adsorption of MV when the visible light irradiation. This result

is described with intrinsic adsorption properties such as surface area and porosity of the photocatalyst sample. The main emphasis here is to show that a more efficient photocatalytic degradation can occur when the catalyst has a larger surface area [48]. An effective degradation value for bare NiS/AC and CoS/AC indicates that activated carbon also plays an effective role. When the degradation results of the composites are examined, higher efficiency is obtained in both the photocatalyst samples. However, in the Ni7Co3/AC sample, the removal is somewhat higher than the other Ni3Co7/AC composite. This result is due to the optimal amount of components in the composite. Optimal content of components achieves excellent balance between visible-light harvesting and charge transfer [49] according to the Langmuir–Hinshelwood equation

$$r = -\frac{dc}{dt} = k \left(\frac{KC}{1 + KC} \right) \quad (8)$$

where r is the reaction rate (ppm/min), k the rate constant, K the Langmuir constant of adsorption, C the MV concentration, and c the MV concentration at any time. At a higher concentration ($KC \gg 1$), the zero-order kinetics occurs due to the catalyst surface being occupied by adsorbed reactant molecules. In contrast ($KC \ll 1$), the reaction rate is related to the initial concentration resulting in the first-order kinetic respectively [11].

In order to reveal the reaction kinetic, $\ln(C_0/C)$ is plotted as a function of the irradiation time and the obtained results are shown in Figure 8(b). It indicates that the pseudo first-order kinetic model shows a better fit. The kinetic rate constant values, k (min^{-1}), are calculated from the slopes of straight line. The obtained kinetic rate constants are shown in Figure 8(b). As seen the kinetic rate constant of the Ni7Co3/AC sample is 3 and 8 times higher than that of Ni3Co7/AC and CoS/AC, respectively. Also, due to the electronic coupling effects with enhanced electronic conductivity between NiS and CoS produce faster charge transportation and surface/interface tuning, and form positive synergistic effect between the NiS and CoS. In addition, AC-supported NiS/CoS composites have an operative mechanical integration due to CoS being better dispersed onto the AC surface and strongly held NiS particles indicating better electronic mobility. As a result, faster diffusion for charge carriers in the photocatalyst system is obtained.

A note of caution is due here (i) band gap energies are very low for both NiS and CoS. Therefore, degradation studies in the dark environment cannot be ignored. (ii) Even negligible, CoS is soluble in water. In this case, the sulphur ions that may arise can change the pH value and may vary in degradation.

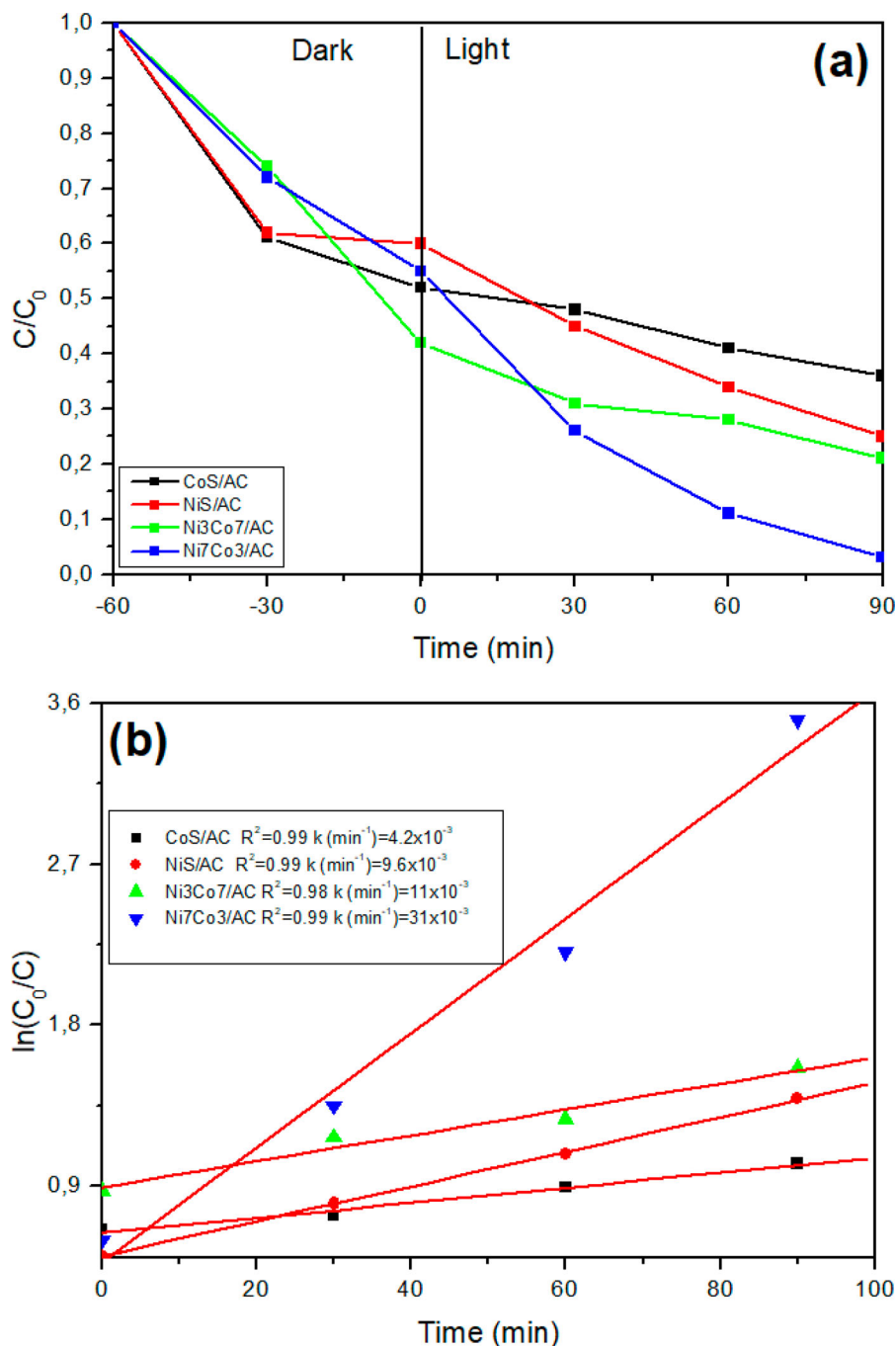


Figure 8. Degradation efficiency (a) pseudo first-order kinetic rate of all photocatalyst samples (b)

3.8. Photocatalytic disinfection performance

The photocatalytic disinfection performance of the Ni₇Co₃/AC composite against *E. coli* (Figure 10) and *P. aeruginosa* (Figure 11) did not show significant change at the end of the incubation period. The Ni₇Co₃/AC composite deactivated 99.99% of *S. aureus* colonies at the end of 2 h (shown in Figure 9 and Table 1). Photocatalytic disinfection efficiency of the Ni₇Co₃/AC composite against *E. faecalis* was reached 100% within 2 h (shown in Figure 12 and Table 1). Ni₇Co₃/AC inactivation performance against *S. aureus* (Figure 9) and *E.*

faecalis (Figure 10) was outstanding; nearly 100% inactivation was attained in less than 2 h. *S. aureus* and *E. faecalis* are both gram positive (Gr+) bacteria. The Ni₇Co₃/AC composite deactivated Gr+ bacteria but had no effect against Gr- bacteria during the incubation period. These results can be attributed to the BET surface area which favourably increases the interfacial interaction between catalytic materials and bacterial cells. In addition, UV-DRS results clearly showed that the visible-light absorption capability of the Ni₇Co₃/AC composite was enhanced to contribute to disinfection effect towards *S. aureus* and *E. faecalis* [50]. According

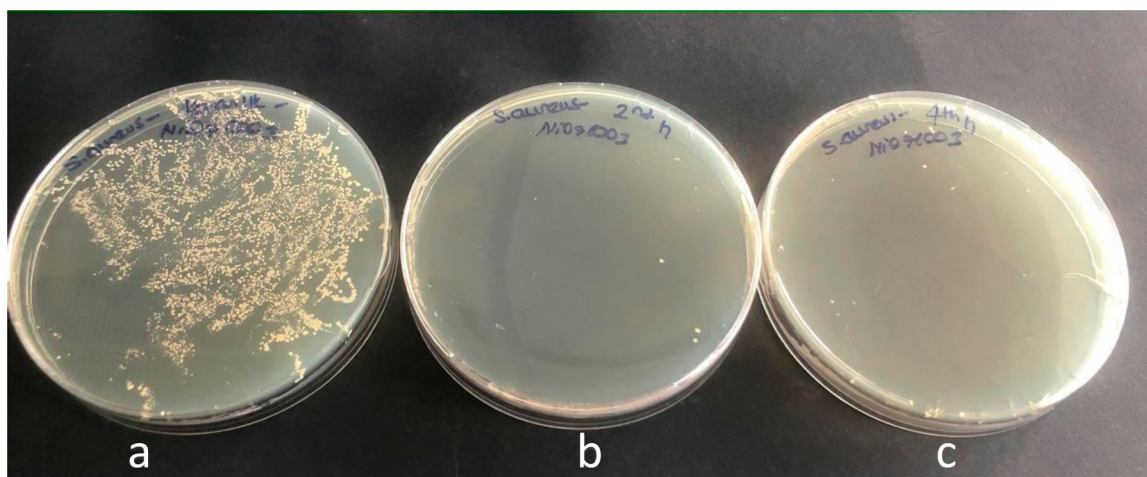


Figure 9. The photocatalytic inactivation of the Ni7Co3/AC composite against *S. aureus* ATCC 25923. (a) Control, (b) 2 h incubation and (c) 4 h incubation.

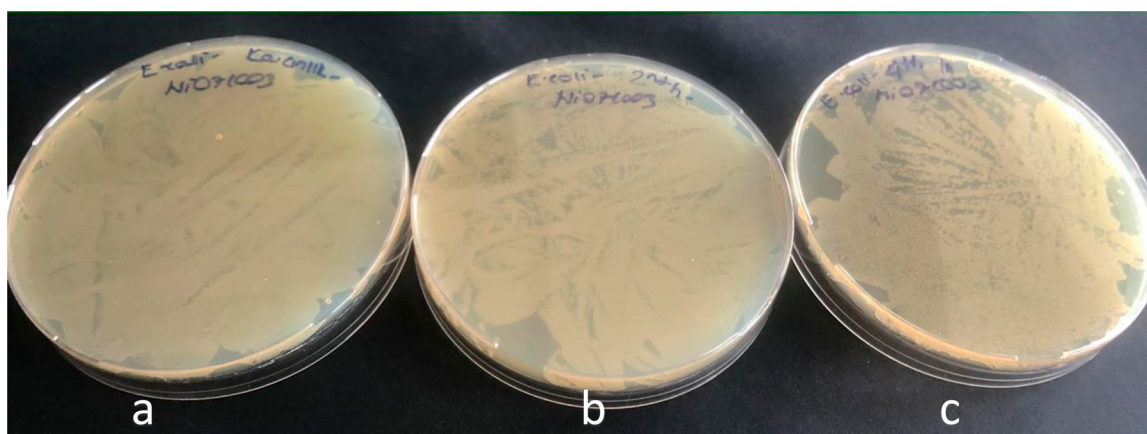


Figure 10. The photocatalytic inactivation of the Ni7Co3/AC composite against *Escherichia coli* ATCC 25922. (a) Control, (b) 2 h incubation and (c) 4 h incubation.

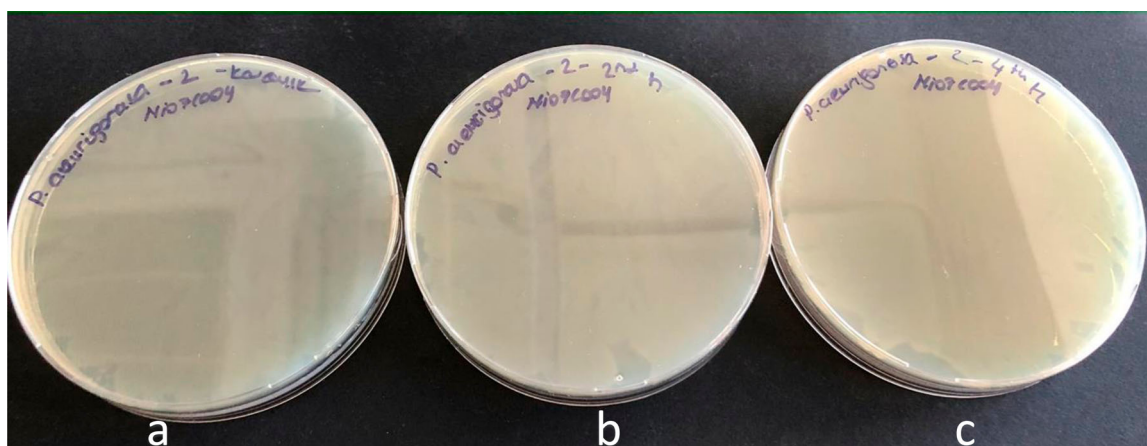


Figure 11. The photocatalytic inactivation of the Ni7Co3/AC composite against *P. aeruginosa* ATCC 27853. (a) Control, (b) 2 h incubation and (c) 4 h incubation.

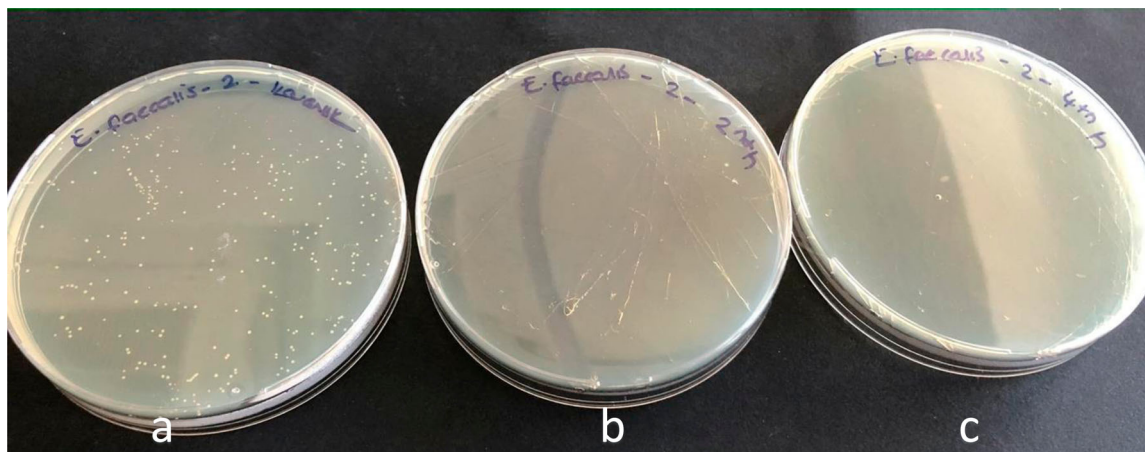


Figure 12. The photocatalytic inactivation of the Ni7Co3/AC composite against *E. faecalis* ATCC 29210. (a) Control, (b) 2 h incubation and (c) 4 h incubation.

Table 1. Microbicide activities of the Ni7Co3/AC composite against *S. aureus* and *E. faecalis* respectively.

Microbicide activities of photocatalyst	2 h Incubation	4 h Incubation
<i>S. aureus</i>	99.9%	99.9%
<i>E. faecalis</i>	100%	100%

to results the composite Ni7Co3/AC failed to destroy the lipopolysaccharide layer of the gram negative (Gr⁻) bacteria cell wall.

4. Conclusion

Composites coupling different semiconductors have attracted increasing attention for photocatalytic application owing to low visible-light absorption capability and weak photocatalytic activity of the single-component system. An efficient sulphur-based nickel and cobalt catalysts were obtained by a simple chemical precipitation method. They were characterized with SEM, XRD, UV-DRS, Raman and PL analysis. The XRD result confirmed the formation of heterojunction. SEM images presented the spherical and very thin platelet NiS and CoS particles, respectively. These materials were then used to decompose the MV dye. During the photocatalytic reaction, the possible degradation pathway was investigated. The findings showed that the amount of NiS is an important parameter. In addition, the degradation efficiency was more increased with the use of activated carbon with a large surface area. The electronic structures of the components also played an active role in achieving this result. The photocatalytic performance of the Ni7Co3/AC sample appears eight times higher than the others. This result in photocatalytic degradation was attributed to large surface area and superior inhibition of charge carries of AC. All findings reveal that the existence of important data in catalytic degradation performance and characterization of sulphur-based nickel and cobalt compounds. The obtained disinfection results showed that

the Ni7Co3/AC composite manifested as an outstanding visible-light-response photocatalyst for the disinfection towards *S. aureus* and *E. faecalis*. According to results, the Ni7Co3/AC composite can be a promising alternative for environmental disinfection under visible-light. It is observed that the synthesized composite Ni7Co3/AC has a performance close to 100% in elimination of Gr⁺ bacteria (*S. aureus* and *E. faecalis*). This research provides new perspectives to the design and development of composites with enhanced photocatalytic activity, which can be inspiring for environmental pollutions.

Disclosure statement

No potential conflict of interest was reported by the author(s).

Funding

This work was supported by Muğla Sitki Koçman University: [Grant Number 15/139].

References

- [1] Li D, Zhang X, Pei L, et al. High-performance super capacitors and non-enzymatic electrochemical glucose sensor based on tremella-like NiS/CoS/NiCo₂S₄ hierarchical structure. *Inorg Chem Commun*. 2019;110:107581.
- [2] Lin T, Chen W, Cai B. Inactivation mechanism of chlorination in *Escherichia coli* internalized in *Limnoithona sinensis* and *Daphnia magna*. *Water Res*. 2016;89:20–27.
- [3] Gao P, Ding Y, Li H, et al. Occurrence of pharmaceuticals in a municipal wastewater treatment plant: mass balance and removal processes. *Chemosphere*. 2012;88:17–24.
- [4] Watson K, Shaw G, Leusch FD, et al. Chlorine disinfection by-products in wastewater effluent: bioassay-based assessment of toxicological impact. *Water Resour*. 2012;46:6069–6083.
- [5] Nyangaresi PO, Qin Y, Chen G, et al. Comparison of UV/LED photolytic and UV-LED/TiO₂ photocatalytic disinfection for *Escherichia coli* in water. *Catal Today*. 2018;335: 200–207. doi:10.1016/j.cattod.2018.11.015.

- [6] Schieppati D, Galli F, Peyot ML, et al. An ultrasound-assisted photocatalytic treatment to remove an herbicidal pollutant from wastewaters. *Ultrason Sonochem.* **2019**;54:302–310.
- [7] Pagga U, Brown D. The degradation of dyestuffs: part II behaviour of dyestuffs in aerobic biodegradation tests. *Chemosphere.* **1986**;15(4):479–491.
- [8] Tamiji T, Nezamzadeh-Ejhieh A. Study of kinetics aspects of the electrocatalytic oxidation of benzyl alcohol in aqueous solution on AgBr modified carbon paste electrode. *Mater Chem Phys.* **2019**;237:121813.
- [9] Xu YS, Zhang WD. Monodispersed Ag_3PO_4 nanocrystals loaded on the surface of spherical Bi_2MoO_6 with enhanced photocatalytic performance. *Dalton Trans.* **2013**;42(4):1094–1101.
- [10] Lewis DM. Coloration in the next century. *Rev Prog Colloid Relat Top.* **1999**;29:23–28.
- [11] Shams-Ghahfarokhi Z, Nezamzadeh-Ejhieh A. As-synthesized ZSM-5 zeolite as a suitable support for increasing the photoactivity of semiconductors in a typical photodegradation process. *Mater Sci Semicond Process.* **2015**;39:265–275.
- [12] Zhang JZ, Yan Y. Synthesis of mesoporous sphere-like copper (I) oxide and its enhancement of Congo red photodegradation performance and CO sensing properties. *J Taiwan Inst Chem Eng.* **2019**;95:405–415.
- [13] Nezamzadeh-Ejhieh A, Khorsandi M. Heterogeneous photodecolorization of Eriochrome Black T using Ni/P zeolite catalyst. *Desalination.* **2010**;262(1-3):79–85.
- [14] Zhou EH, Hu W, Ding Q, et al. Photocatalytic decontamination of methyl violet by a 3D twofold interpenetrating metal-organic framework. *Inorg Chem Commun.* **2020**;120:108155.
- [15] Foroutan R, Mohammadi R, MousaKhanloo F, et al. Performance of montmorillonite/graphene oxide/ CoFe_2O_4 as a magnetic and recyclable nanocomposite for cleaning methyl violet dye-laden wastewater. *Adv Powder Technol.* **2020**;31(9):3993–4004.
- [16] Fujimori A, Mamiya K, Mizokawa T, et al. Resonant photoemission study of pyrite-type NiS_2 , CoS_2 and FeS_2 . *Phys Rev B.* **1996**;54(23):16329–16332.
- [17] Rahmani-Aliabadi A, Nezamzadeh-Ejhieh A. A visible light $\text{FeS}/\text{Fe}_2\text{S}_3/\text{zeolite}$ photocatalyst towards photodegradation of ciprofloxacin. *J Photochem Photobiol A.* **2018**;357:1–10.
- [18] Derikvandi H, Nezamzadeh-Ejhieh A. Designing of experiments for evaluating the interactions of influencing factors on the photocatalytic activity of NiS and SnS_2 : focus on coupling, supporting and nanoparticles. *J Colloid Interface Sci.* **2017**;490:628–641.
- [19] Derikvandi H, Nezamzadeh-Ejhieh A. Synergistic effect of pn heterojunction, supporting and zeolite nanoparticles in enhanced photocatalytic activity of NiO and SnO_2 . *J Colloid Interface Sci.* **2017**;490:314–327.
- [20] González-Casamachin DA, De la Rosa JR, Lucio-Ortiz CJ, et al. Visible-light photocatalytic degradation of acid violet 7 dye in a continuous annular reactor using ZnO/PPy photocatalyst: synthesis, characterization, mass transfer effect evaluation and kinetic analysis. *Chem Eng J.* **2019**;373:325–337.
- [21] Derikvandi H, Nezamzadeh-Ejhieh A. Comprehensive study on enhanced photocatalytic activity of heterojunction $\text{ZnS}-\text{NiS}/\text{zeolite}$ nanoparticles: experimental design based on response surface methodology (RSM), impedance spectroscopy and GC-MASS studies. *J Colloid Interface Sci.* **2017**;490:652–664.
- [22] Fu Z, Zhao X, Zhang S, et al. Preparation of nano- $\text{Zn}_2\text{GeO}_4/\text{rGO}$ composite photocatalyst and its treatment of synthetic dye wastewater. *Mater Chem Phys.* **2021**;259:124004.
- [23] Borthakur P, Das MR. Hydrothermal assisted decoration of NiS_2 and CoS nanoparticles on the reduced graphene oxide nanosheets for sunlight driven photocatalytic degradation of azo dye: effect of background electrolyte and surface charge. *J Colloid Interface Sci.* **2018**;516:342–354.
- [24] Yang Y, Zhang Y, Zhou Y, et al. Design and synthesis of $\text{NiS}@ \text{CoS}@ \text{CC}$ with abundant heterointerfaces as high-efficiency hydrogen evolution electrocatalyst. *Int J Hydrogen Energy.* **2019**;44(49):26753–26763.
- [25] Habibi-Yangjeh A, Asadzadeh-Khaneghah S, Feizpoor S, et al. Review on heterogeneous photocatalytic disinfection of waterborne, airborne, and foodborne viruses: can we win against pathogenic viruses? *J Colloid Interface Sci.* **2020**;580(15):503–514.
- [26] Clinical and Laboratory Standards Institute (CLSI). Methods for dilution antimicrobial susceptibility tests for bacteria that grow aerobically, approved Standard M7-A7. 7th ed. Wayne (PA): CLSI; **2006**.
- [27] Yan D, Wu X, Pei J, et al. Construction of $g\text{-C}_3\text{N}_4/\text{TiO}_2/\text{Ag}$ composites with enhanced visible-light photocatalytic activity and antibacterial properties. *Ceram Int.* **2020**;46(1):696–702.
- [28] Morales-Leal FJ, De la Rosa JR, Lucio-Ortiz CJ, et al. Comparison between the catalytic and photocatalytic activities of $\text{Cu}/\text{Al}_2\text{O}_3$ and TiO_2 in the liquid-phase oxidation of methanol-ethanol mixtures: development of a kinetic model for the preparation of catalyst. *Appl Catal, A.* **2018**;562:184–197.
- [29] Gong J, Zhang J, Lin H, et al. “Cooking carbon in a solid salt”: synthesis of porous heteroatom-doped carbon foams for enhanced organic pollutant degradation under visible light. *Appl Mater Today.* **2018**;12:168–176.
- [30] Samaniego-Benitez JE, Jimenez-Rangel K, Lartundo-Rojas L, et al. Enhanced photocatalytic H_2 production over $g\text{-C}_3\text{N}_4/\text{NiS}$ hybrid photocatalyst. *Mater Lett.* **2021**;290:129476.
- [31] He HY. Efficient interface-induced effect of novel reduced graphene oxide- CoS hetero-nano-structures in enhancing photocatalytic activities. *Appl Surf Sci.* **2017**;421:260–267.
- [32] Pourshirband N, Nezamzadeh-Ejhieh A, Mirsattari SN. The coupled AgI/BiOI catalyst: synthesis, brief characterization, and study of the kinetic of the EBT photodegradation. *Chem Phys Lett.* **2020**;761:138090.
- [33] Tamiji T, Nezamzadeh-Ejhieh A. A comprehensive study on the kinetic aspects and experimental design for the voltammetric response of a $\text{Sn (IV)-clinoptilolite}$ carbon paste electrode towards Hg (II) . *J Electroanal Chem.* **2018**;829:95–105.
- [34] Shombe GB, Khan MD, Zequine C, et al. Direct solvent free synthesis of bare $\alpha\text{-NiS}$ $\beta\text{-NiS}$ and $\alpha\text{-}\beta\text{-NiS}$ composite as excellent electrocatalysts: effect of self-capping on supercapacitance and overall water splitting activity. *Sci Rep.* **2020**;10(1):1–14.
- [35] Cant DJ, Syres KL, Lunt PJ, et al. Surface properties of nanocrystalline PbS films deposited at the water-oil interface: a study of atmospheric aging. *Langmuir.* **2015**;31(4):1445–1453.
- [36] Liu J, Lin H, He Y, et al. Novel $\text{CoS}_2/\text{MoS}_2@ \text{zeolite}$ with excellent adsorption and photocatalytic performance for tetracycline removal in simulated wastewater. *J Clean Prod.* **2020**;260:121047.

- [37] Johra FT, Lee JW, Jung WG. Facile and safe graphene preparation on solution based platform. *J Ind Eng Chem.* **2014**;20(5):2883–2887.
- [38] Nosuhi M, Nezamzadeh-Ejhieh A. High catalytic activity of Fe(II)-clinoptilolite nanoparticules for indirect voltammetric determination of dichromate: experimental design by response surface methodology (RSM). *Electrochim Acta.* **2017**;223:47–62.
- [39] Amani-Beni Z, Nezamzadeh-Ejhieh A. Nio nanoparticles modified carbon paste electrode as a novel sulfasalazine sensor. *Anal Chim Acta.* **2018**;1031:47–59.
- [40] Chen Z, Yang S, Tian Z, et al. Nis and graphene as dual cocatalysts for the enhanced photocatalytic H₂ production activity of g-C₃N₄. *Appl Surf Sci.* **2019**;469:657–665.
- [41] Zhang Z, Zhao H, Zeng Z, et al. Hierarchical architected NiS@SiO₂ nanoparticles enveloped in graphene sheets as anode material for lithium ion batteries. *Electrochim Acta.* **2015**;155:85–92.
- [42] Zhu Y, Li J, Yun X, et al. Graphitic carbon quantum dots modified nickel cobalt sulfide as cathode materials for alkaline aqueous batteries. *Nano-Micro Lett.* **2020**;12(1):1–18.
- [43] Ma D, Hu B, Wu W, et al. Highly active nanostructured CoS₂/CoS heterojunction electrocatalysts for aqueous polysulfide/iodide redox flow batteries. *Nat Commun.* **2019**;10(1):1–8.
- [44] Derikvandi H, Nezamzadeh-Ejhieh A. Increased photocatalytic activity of NiO and ZnO in photodegradation of a model drug aqueous solution: effect of coupling, supporting, particles size and calcination temperature. *J Hazard Mater.* **2017**;321:629–638.
- [45] Ghattavi S, Nezamzadeh-Ejhieh A. A visible light driven AgBr/g-C₃N₄ photocatalyst composite in methyl orange photodegradation: focus on photoluminescence, mole ratio, synthesis method of g-C₃N₄ and scavengers. *Compos Part B Eng.* **2020**;183:107712.
- [46] Vaizoğullar Aİ. An effective photocatalytic and photoelectrochemical performance of β/γ -MnS/CdS composite photocatalyst for degradation of flumequine and oxytetracycline antibiotics under visible light irradiation. *J Mater Sci.* **2020**;55(9):4005–4016.
- [47] Raeisi-Kheirabadi N, Nezamzadeh-Ejhieh A. A Z-scheme g-C₃N₄/Ag₃PO₄ nanocomposite: its photocatalytic activity and capability for water splitting. *Int J Hydrogen Energy.* **2020**;45(58):33381–33395.
- [48] Luo S, Liu C, Zhou S, et al. ZnO nanorod arrays assembled on activated carbon fibers for photocatalytic degradation: characteristics and synergistic effects. *Chemosphere.* **2020**;261:127731.
- [49] Ren D, Liang Z, Ng YH, et al. Strongly coupled 2D-2D nanojunctions between P-doped Ni₂S (Ni₂SP) cocatalysts and CdS nanosheets for efficient photocatalytic H₂ evolution. *Chem Eng J.* **2020**;390:124496.
- [50] Ji L, Liu B, Qian Y, et al. Enhanced visible-light-induced photocatalytic disinfection of *Escherichia coli* by ternary Bi₂WO₆/TiO₂/reduced graphene oxide composite materials: insight into the underlying mechanism. *Adv Powder Technol.* **2020**;31(1):128–138.